HHS Public Access

Author manuscript

Cell. Author manuscript; available in PMC 2018 January 26.

Published in final edited form as:

Cell. 2017 January 26; 168(3): 487–502.e15. doi:10.1016/j.cell.2016.12.022.

Systemic Immunity is Required for Effective Cancer Immunotherapy

Matthew H. Spitzer[1,2,3,4,6,7,8], **Yaron Carmi**[1,6], **Nathan E. Reticker-Flynn**[1,6], **Serena S. Kwek**[5], **Deepthi Madhireddy**[2], **Maria M. Martins**[1], **Pier Federico Gherardini**[2], **Tyler R. Prestwood**[1], **Jonathan Chabon**[1], **Sean C. Bendall**[1], **Lawrence Fong**[5], **Garry P. Nolan**[2,3,7], and **Edgar G. Engleman**[1,3,7]

[1]Department of Pathology, Stanford University, Stanford, CA, USA

[2]Baxter Lab in Stem Cell Biology, Department of Microbiology and Immunology, Stanford University, Stanford, CA, USA

[3]Program in Immunology, Stanford University, Stanford, CA, USA

[4]Department of Microbiology and Immunology, University of California, San Francisco, CA, USA

[5]Department of Medicine, Hem/Onc Division, University of California, San Francisco, CA, USA

Summary

Immune responses involve coordination across cell types and tissues. However, studies in cancer immunotherapy have focused heavily on local immune responses in the tumor microenvironment. To investigate immune activity more broadly, we performed an organism-wide study in genetically-engineered cancer models using mass cytometry. We analyzed immune responses in several tissues after immunotherapy by developing intuitive models for visualizing single-cell data with statistical inference. Immune activation was evident in the tumor and systemically shortly after effective therapy was administered. However, during tumor rejection, only peripheral immune cells sustained their proliferation. This systemic response was coordinated across tissues and required for tumor eradication in several immunotherapy models. An emergent population of peripheral CD4 T cells conferred protection against new tumors and was significantly expanded in patients responding to immunotherapy. These studies demonstrate the critical impact of systemic immune responses that drive tumor rejection.

Correspondence: matthew.spitzer@ucsf.edu (M.H.S.), edengleman@stanford.edu (E.G.E.).
[6]Co-first authors
[7]Corresponding authors
[8]Lead contact

Author Contributions

Conceptualization, M.H.S., Y.C., N.R.F.; Experimental Methodology, M.H.S., Y.C., N.R.F., S.S.K; Computational Methodology, M.H.S., P.F.G.; Investigation, M.H.S., Y.C., N.R.F., S.S.K., D.M., M.M.M., T.R.P., J.C., L.F.; Writing – Original Draft, M.H.S.; Writing – Review & Editing, all authors; Funding Acquisition, M.H.S., S.C.B., L.F., G.P.N., E.G.E.; Resources, S.C.B.; Supervision, L.F., G.P.N., E.G.E.

eTOC

A systems approach reveals that engagement of systemic immunity is critical to the process of tumor rejection following immunotherapy

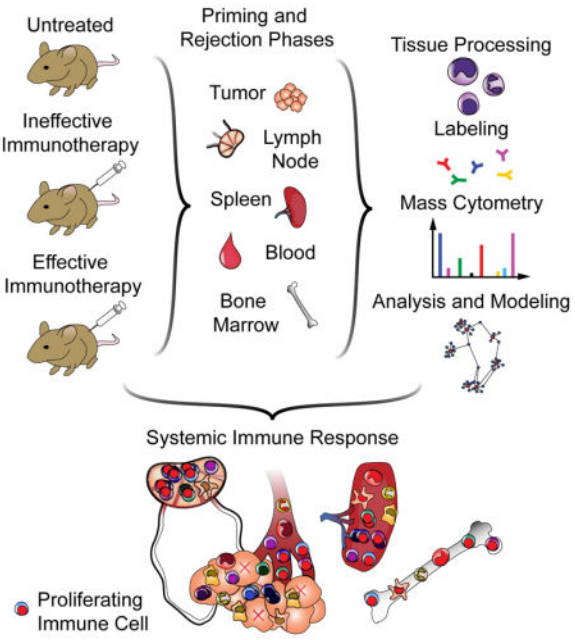

Introduction

Since the use of bacterial vaccines for the treatment of cancer over a century ago (Coley, 1893), evidence has mounted demonstrating the ability of the immune system to reject tumors. Several immunotherapeutic strategies have now yielded sustained clinical responses, including blocking antibodies against suppressive receptors (Topalian et al., 2015) and transfer of adoptive T cells (Restifo et al., 2012), dendritic cells (Kantoff et al., 2010), or engineered T cells (Porter et al., 2011). For specific immunotherapies, individual cell subsets have been queried for mechanistic roles, and features have been correlated with responsiveness (Herbst et al., 2014). However, a comprehensive understanding of the global immune dynamics that mediate effective anti-tumor immunity remains unclear. Because most cancer patients do not respond to immunotherapy, there is an urgent need to improve upon the current toolkit, especially for adenocarcinomas, the most common forms of cancer.

Another gap in our knowledge is which anatomic sites drive anti-tumor immunity. Expansion of tumor-infiltrating T cells has shown striking results in melanoma, demonstrating that effective cells can be found within the microenvironment (Restifo et al., 2012). In contrast, dendritic cell vaccines can stimulate *de novo* T cell responses and have shown efficacy (Kantoff et al., 2010). For strategies that initiate anti-tumor immunity in the patient, it remains unclear where immune cell activation takes place. For example, in the case of CTLA-4 blockade, administering antibody into the tumor can induce rejection (Simpson et al., 2013) and is dependent on Fcγ receptors (Bulliard et al., 2013), consistent with depleting intratumoral regulatory T cells and releasing local effector cells. However,

new tumor-reactive T cell clones emerge in patients experiencing clinical benefit, suggestive of new priming (Kvistborg et al., 2014). For other strategies to induce immune responses *in situ*, this question has not been addressed conclusively.

New methods of assessing the immune state under any given condition allow us to systematically address this question by characterizing diverse cell subsets and their activation states simultaneously. Mass cytometry builds upon the success of flow cytometry and enables over 40 simultaneous parameters to be quantified by replacing fluorophores with mass tags (Bandura et al., 2009; Bendall et al., 2011). It is thus possible to discern the identity and behavior of numerous cell types from a single experiment (Bendall et al., 2011; Spitzer et al., 2015). Using a spontaneous model of triple-negative breast cancer, we assessed immune cell dynamics across the organism during tumor rejection.

Results

Tumor-binding antibodies combined with dendritic cell adjuvants induce potent T cell immunity against spontaneous breast tumors

To characterize effective anti-tumor immunity, we chose a therapy with efficacy in multiple cancer types. We recently described the combination of tumor-binding antibodies and adjuvants to stimulate dendritic cells as a means of inducing potent T cell-mediated immunity (Carmi et al., 2015). Beyond melanomas, this strategy was effective against Lewis lung and 4T1 breast carcinomas. While carcinomas are the most common class of cancer, more limited progress has been made in immunotherapy compared to melanoma or hematological malignancies (Topalian et al., 2015). We thus determined if this approach would be effective in a widely used spontaneous model of carcinoma, MMTV-PyMT triple-negative breast cancer, which is refractory to other immunotherapies such as checkpoint blockade (i.e., anti-PD-1) (Bos et al., 2013).

Once animals developed a tumor of 25mm^2, they were injected intratumorally with allogeneic tumor-binding IgG antibodies (alloIgG) combined with anti-CD40 antibody and interferon (IFN)-γ (Carmi et al., 2015). Treated animals experienced regression of the injected lesion (Fig. 1A). We previously established that the efficacy of this therapy in melanoma depends on T cell responses. Treated MMTV-PyMT tumors were infiltrated by CD8 T cells, concurrent with tumor shrinkage and tumor cell death indicated by TUNEL staining (Fig. 1B–C).

We devised an experimental strategy for elucidating the system-wide immunological underpinnings of this response (Fig. 1D). AlloIgG from CD-1 and C57BL/6 mice bound MMTV-PyMT breast tumor cells (Fig. 1E). Mice were randomized to one of those sources of alloIgG, ensuring that responses were not specific to one antibody source. Anti-PD-1 served as a model of ineffective therapy due to its wide clinical use but lack of efficacy in this model. PyMT-expressing females were randomized to treatment groups as follows: B6-alloIgG + anti-CD40 + IFNγ, CD-1-allo-IgG + anti-CD40 + IFNγ, anti-PD-1, or no treatment. The mouse began treatment once it developed a tumor of 25 mm^2, which was considered day zero.

We previously determined that immune activation is discernable by 3 days after treatment (i.e., “priming phase”), with tumor shrinkage by day 8 (i.e., “rejection phase”). At these time points, we sacrificed mice from each treatment (n=3–4 per treatment, per time point) and prepared tissues for mass cytometry. Animals receiving alloIgG therapy experienced significant tumor regression by day 8, with no significant difference between untreated animals and those receiving anti-PD-1 (Fig. 1F). This design enabled us to contrast effective and ineffective immune responses.

Immune cell proliferation is not maintained in the tumor microenvironment during tumor rejection

We next sought to systematically define changes in immune cell organization and behavior in the tumor microenvironment between the effective and ineffective treatments. We recently reported a computational method called Scaffold maps for creating a reference map from high-dimensional single-cell data, facilitating comparisons across samples (Spitzer et al., 2015). These maps provide a data-driven representation of the cells present in a sample while also denoting the location of landmark immune cell populations, defined using prior knowledge of the immune system (Fig. S1). These Landmarks (visualized as black nodes in the graph) function as flags to orient the investigator. In these graphs, the similarity of two groups of cells is visualized by the length of the edge connecting them. In other words, two groups of cells connected by a short line are similar to one another with respect to the proteins they express (see Methods).

This method was developed in an extensible manner for future datasets to be incorporated, but it did not enable precise statistical comparisons across groups of samples. Another algorithm for mass cytometry analysis, Citrus (Bruggner et al., 2014), provides statistical comparisons between groups. The results from Citrus, however, can be cumbersome to interpret. We therefore determined whether the statistical inference integrated into Citrus could instead be applied to Scaffold maps. We call this hybrid method “Statistical Scaffold” (Fig. S1). We altered the first step of Scaffold maps, clustering data from all tumor specimens together to define cell groups in an unbiased manner. This enables direct comparisons across samples. We then used the Significance Analysis of Microarrays framework to identify statistically significant features between the sample types (effective vs. ineffective treatment groups) as in Citrus (Bair and Tibshirani, 2004; Bruggner et al., 2014). The resulting Scaffold maps can then be colored by statistical significance, where features with q-values less than 0.05 (adjusted for multiple testing) are colored in either red or blue depending on the directionality of the change (for example, up or down in the group that received effective therapy). These features can either be changes in the frequency or molecular expression of a particular cell subset.

Because the text identifying Landmark populations can be obscured, an empty reference graph can be found as Fig. S2. The frequency, coefficient of variation and protein expression of each cluster are shown in Fig. S3 and Table S2. Because the plasmacytoid dendritic cells (pDC) are far from other cell populations in the graph, they are displayed in an inset image (black dashed outline).

We began applying Statistical Scaffold to data from the tumor specimens collected during the priming phase. In animals treated with effective therapies, a large number of immune cells increased in frequency as a percent of total cells in the tumor, consistent with an anti-tumor immune response (Fig. 2A). Very few differences existed between untreated mice and those receiving the ineffective anti-PD-1 therapy (Fig. S2B–D), demonstrating that effective therapy initiated a fundamentally different immune response. We therefore asked how these cell populations were changing with effective therapy at the molecular level, leveraging the interactivity of Scaffold maps to visualize protein expression between the treatment groups.

Subsets of macrophages increasing in frequency with effective treatment expressed high levels of the immunosuppressive co-receptor programmed death-ligand 1 (PD-L1) and plasmacytoid dendritic cell antigen 1 (PDCA-1), both of which are inducible by IFNγ. Additionally, these cells had high expression of the co-stimulatory receptor CD86 and MHC class II, indicating activation and enhanced antigen presentation. A small decrease in expression of Fcγ receptors (FcγR) CD16/32 could reflect internalization upon ligation by alloIgG (Fig. 2B).

Classical dendritic cells (cDC) increasing during the priming phase also expressed high levels of CD86, MHC II and PD-L1 (Fig. 2C). The integrin CD103 mediates trafficking to the tissues and is expressed by cross-presenting DC that can promote anti-tumor immunity (Broz et al., 2014). Interestingly, this population significantly decreased in tumors after effective therapy, perhaps indicating migration. DC increasing in frequency after effective therapy displayed higher variance in FcγR CD16/32 expression, consistent with modulation of this pathway during effective therapy with alloIgG. Concurrently, there was also an unexpected increase in myeloid populations traditionally thought to be immunosuppressive in cancer, such as $Ly6C^+$ monocytes and $Ly6G^+$ neutrophils (Gabrilovich et al., 2012).

NK cell subsets markedly increased with higher expression of CD11b, killer-cell lectin like receptor G1 (KLRG1), and the transcription factor T-bet, consistent with an effector phenotype (Fig. 2D). These cells had little expression of the immunosuppressive co-receptor programmed death-1 (PD-1).

Several types of T cells expanded significantly with effective therapy. Several increasing subsets were attributable to conventional CD4 and CD8 T cells. Contrary to expectations, however, regulatory T cells (Tregs) expressing the transcription factor Foxp3 were also more prevalent after effective therapy (Fig. 2E). These cells co-expressed KLRG1 and CD44, denoting an increase in effector Tregs (Cheng et al., 2012) present in the tumor. The frequency of Tregs has been suggested as a negative prognostic feature for various tumors (Bates et al., 2006; Curiel et al., 2004). Based on our data, utilizing this metric would be quite misleading. Taken together, these results demonstrate the complex dynamics that underlie productive anti-tumor immunity, including the effector and regulatory arms of myeloid and lymphoid lineages.

We next queried whether changes in immune cell proliferation within the tumor were observed. During the priming phase, a large portion of immune cell types exhibited increased rates of proliferation with effective therapies, evident by the proportion of cells

expressing Ki67 (Fig. 2F), including Tregs (Fig. 2G). Despite decreasing in frequency, CD103+ DC also exhibited higher proliferation (Fig. 2H), suggesting that these cells do become activated. Thus, the priming phase of the effective anti-tumor immune response is characterized by broad expansion of leukocytes as well as enhanced proliferation in the tumor microenvironment across many immune cell types.

We next mapped the dynamics of intratumoral immune cells during the rejection phase (8 days after therapy)(Fig. 2I). Similar changes to those seen in the priming phase were observed in the macrophage compartment during tumor rejection, consistent with activation (Fig. 2J). The frequency of B cell subsets and innate lymphoid cells (ILC) also increased during the rejection phase. One prominent ILC cluster (outlined in orange) contained cells expressing FcγR, some of which expressed T-bet (Fig. 2K). Manual identification of T-bet+ type-1 ILC confirmed their increased prevalence (Fig. 2L). Numerous clusters of T cells were also significantly expanded with effective therapy, including effector memory CD4 and CD8 T cells (Fig. 2M–N) as well as Tregs.

In stark contrast to the priming phase, there was no difference in the rate of proliferation across immune cells in the tumor microenvironment during the rejection phase (Fig. 2O). Similar results were found in a genetically-engineered inducible mouse model of melanoma driven by $Braf^{V600E}$ and loss of Pten (referred to as BP melanoma mice) on day eight after treatment with effective therapy (Fig S3A)(Dankort et al., 2009). We therefore hypothesized that other anatomical locations were responsible for sustaining the immune response during the rejection phase.

Lymphocyte activation and proliferation are maintained in the secondary lymphoid organs throughout the immune response

We next analyzed the immune cell composition in the tumor-draining lymph nodes of treated animals. During the priming phase, several specific clusters of lymphocytes expanded in frequency (Fig. 3A). Marked expansion of activated, naive B cells expressing IgM, high levels of CD44, CD86 and MHC II, but low levels of IgD, was observed (Fig. 3B).

In the T cell compartment, a cluster of Th1 cells (CD44+T-bet+) emerged with effective therapy with a unique phenotype ($CD90^{hi}$CD69+CD62L-CD27-KLRG1-) and active proliferation (Ki-67+)(Fig. 3C). Additionally, a Treg subset with a similar molecular profile to intratumoral Tregs ($KLRG1^{hi}$CD103+) significantly expanded (Fig. 3D). The CD8 T cells that became more prevalent with effective therapy had some features of central memory cells (Ly6C+ and CD62L+), though they did not upregulate CD44 expression (Fig. 3E)(Hänninen et al., 2011; Wherry et al., 2007).

Analysis of proliferation in the draining lymph node revealed active cell division across many cell types during the priming phase of an effective anti-tumor immune response (Fig. 3F). Nearly all clusters of B cells, NK cells, cDC, plasmacytoid DC (pDC) and ILC displayed enhanced Ki67 expression. Effector/memory T cell clusters (CD44+ or Ly6C+) exhibited significant increases in proliferation (Fig. 3G), consistent with the development of a T cell-mediated immune response.

The rejection phase in the tumor-draining lymph node displayed similarly complex dynamics (Fig. 3H). Similar changes in the B cell compartment were observed as during the initiation phase (Fig. 3I), which may in part be in response to anti-CD40. Both increasing CD4 and CD8 T cell subsets exhibited higher expression of CD62L without a change in PD-1 levels (Fig. 3J–K). A subset of expanding CD8 T cells also expressed Ly6C and CD44 (Fig. 3K), denoting the formation of central memory CD8 T cells. Consistent with the tumor microenvironment, Tregs also increased in frequency (Fig. 3L), once again highlighting immune regulation.

In contrast to the tumor microenvironment, however, significant increases in leukocyte proliferation across the system were observed during the rejection phase in the draining lymph node (Fig. 3M). This observation was also consistent in BP melanoma mice after therapy (Fig. S4B). Furthermore, this trend extended to some naïve T cell subsets that had not increased their rates of division during the priming phase (Fig. 3M). These dynamics, with elevated proliferation of antigen-experienced cells followed by naïve cells, suggest that previously activated T cell clones form a memory immune response, followed by a wave of *de novo* T cell activation. These results conclusively demonstrate that immune cell proliferation persists in the periphery, even after cells in the tumor microenvironment return to baseline levels of cell division.

We next asked if the immune response extended into other secondary lymphoid organs such as the spleen, where contact with the treated tumor was less direct. Similar changes were observed in the priming and rejection phases (Fig. S5A,H), including expansion of activated B cells (Fig. S5B,I). Plasma cells also increased in frequency, proliferating and upregulating MHC II, which has been associated with regulation of T cell responses (Fig. S5C,J)(Pelletier et al., 2010). The T cell and NK cell compartments in the spleen also changed similarly (Fig. S5D–F,K–M), including the emergence of a CD90^{hi}Ki-67+ Th1 cell population (Fig. S5E). Proliferation in the spleen was also widespread during priming and rejection (Fig. S5G,N), demonstrating that sustained proliferation is generalizable across secondary lymphoid organs during effective anti-tumor immunity.

Systemic activation during effective immunotherapy is captured in peripheral blood

To assess whether the responses we observed during tumor rejection were indeed systemic, we analyzed peripheral blood. Profound changes were apparent during the priming phase (Fig. 4A). NK cells, cDC activated B cells and a subset of activated pDC (Ly6C+CD4+MHC II^{hi}) all increased in frequency (Fig. 4B–C). Changes in the T cells paralleled those of the secondary lymphoid organs. CD4 T cell subsets increasing in frequency were largely naïve cells (CD62L+CD44−) with no change in PD-1 levels (Fig. 4D). The emergence of CD90^{hi} proliferative Th1 cells was also evident (Fig. 4E). CD8 T cells increasing in frequency were antigen-experienced cells expressing Ly6C and variable levels of CD44 (Fig. 4F). Alterations in circulating monocytes were observed, with subsets of classical (Ly6C^{+}) and non-classical (Ly6C^{-}) monocytes expressing elevated levels of F4/80, the CSF-1 receptor (CD115), MHC II and PD-L1, indicative of activation and perhaps differentiation to a macrophage-like state (Fig. 4G–H). Many cell types exhibited increased proliferation as well (Fig. 4I), including macrophages, cDC, pDC, B cells, NK cells, and many T cell clusters,

particularly effector/memory cells. These results support the notion that the priming phase of the anti-tumor immune response is systemic in nature.

The rejection phase in the blood was marked by more substantial decreases in immune cell frequencies (Fig. 4J) and an increase in platelet frequencies (Fig. 4K). These dynamics may reflect immune cells trafficking into the tissues., Many immune cell populations retained elevated levels of proliferation during the rejection phase (Fig. 4L), demonstrative of ongoing immune responses in circulating cells. This was also observed in BP melanoma mice (Fig. S4C). This sustained immune cell proliferation in the blood may present opportunities for non-invasive immune monitoring of anti-tumor immunity.

Immune remodeling by effective immunotherapy extends to the bone marrow

Because the immune response was evidently systemic, we asked whether changes might also take place in the bone marrow, thereby affecting hematopoiesis. Similarly widespread changes were evident (Fig. S6A,I), involving the emergence of activated B cells, CD4 and CD8 T cells, macrophages and pDC (Fig. S6B–F,J–N). No changes were observed in the frequency of hematopoietic progenitors (Lineage-cKit+ cells), however (Fig. S6G,O). Many T cell, B cell, and DC subsets exhibited more proliferation during both the initiation and rejection phases (Fig. S6H,P), reflecting a truly systemic response.

Systemic immune responses are required for tumor eradication

Effective immunotherapy induces marked changes in both the microenvironment and the periphery, but the prevailing dogma holds that productive immunotherapy functions by reinvigorating immune cells that are actively suppressed in the tumor microenvironment (Jiang et al., 2015). We thus sought to clarify the predominant site in which the anti-tumor immune response was generated. To segregate the immune response in the tumor from the systemic immune response, we treated animals with FTY720, a ligand of the sphinosine-1-phosphate receptor 1, which is required for immune cells to migrate from the secondary lymphoid organs (Matloubian et al., 2004). Treatment was initiated one day prior to immunotherapy to inhibit migration caused by immunotherapy. Animals treated with vehicle control and immunotherapy experienced tumor regression, but those co-administered FTY720 had progressive tumor growth (Fig. 5A). Therefore, we conclude that the local activation of tumor-infiltrating leukocytes is insufficient to mediate tumor rejection in this system, instead pointing to an essential role for the systemic immune response.

We previously reported that tumor-binding antibody therapy induces tumor-eradicating immune responses in the transplantable 4T1 breast cancer model (Carmi et al., 2015). Consistent with the autochthonous model, blocking leukocyte egress from lymphoid organs prevented regression of 4T1 tumors as well (Fig. 5B). Treating these mice again on day 7 after the initial dose resulted in modest tumor shrinkage followed by continued growth, demonstrating that the kinetics of the response were not simply altered by inhibiting leukocyte egress (Fig. 5B). Consistently, histological analysis of tumors revealed robust T cell infiltration in animals treated with tumor-binding antibody therapy alone, while simultaneous inhibition of leukocyte egress prevented accumulation of CD4 and CD8 T cells

but not CD11b+ myeloid cells (Fig. 5C). Inhibition of leukocyte egress also prevented immunological control of metastasis to the lungs (Fig. 5D–E).

Finally, we assessed whether the T cells in the secondary lymphoid organs were sufficient to induce anti-tumor immunity. After tumor-binding antibody therapy with egress blockade, T cells were transferred from the secondary lymphoid organs into naïve animals, which were challenged with 4T1 tumor cells the following day. Consistent with our previous findings, these T cells from the periphery were sufficient to confer protection from 4T1 tumors (Fig. 5F). These results rule out the possibility that FTY720 directly prevented the anti-tumor activity of T cells and demonstrate that anti-tumor T cells are induced in the secondary lymphoid organs during the immune response.

Tumor-binding antibody therapy functions by enabling dendritic cell-mediated activation of T cells (Carmi et al., 2015). In contrast, the rejuvenation of exhausted T cells has been suggested as a primary mechanism underlying other immunotherapies, such as checkpoint blockade with anti-PD-1 antibodies (Topalian et al., 2015). We thus determined whether T cell responses in the lymphoid organs were required for productive anti-PD-1 therapy as well. Treatment of mice bearing MC38 colon carcinomas with anti-PD-1 antibodies did induce anti-tumor immune responses capable of controlling tumor growth for up to two weeks (Fig. 5G). In contrast, tumors in animals treated with anti-PD-1 and FTY720 grew progressively, similar to untreated animals (Fig. 5G). These results demonstrate that a systemic immune response is required for effective immunotherapy across multiple cancer models and therapeutic strategies.

A peripheral CD4 T cell subset confers protection to new tumors

Having established a requirement for peripheral immune responses and previously determined that tumor eradication initiated by tumor-binding antibody therapy is T cell-dependent (Carmi et al., 2015), we asked whether we could identify the peripheral T cell subsets that drove tumor eradication. Network analyses have proven effective for identifying dominant elements of a systems-level response (Hotson et al., 2012; Ideker and Krogan, 2012). We therefore calculated immune cell population frequencies from each tissue and calculated pairwise correlations across all animals receiving effective therapy. Indeed, several coordinated modules were readily apparent (Fig. 6A). While many immune features in the tumor were concentrated in a single module, features from peripheral tissues were interspersed, demonstrating coordination across organs during the productive immune response. This was especially evident among effector/memory T cell subsets in the peripheral sites (Fig. S7A). These modules did not simply represent basal organization at steady-state (Fig. S7B–C), confirming that effective immunotherapy involves new systemic coordination of an immune response.

To identify the key T cell populations that may coordinate the response, we assessed the degree of connectivity of each subset. We generated an adjacency matrix, filtering out weak correlations, and ranked populations by their connectivity in the network. Of the T cell subpopulations, seven of the top eight ranking subsets were types of CD4 T cells (Fig. 6B). We thus hypothesized that CD4 T cells were more central to the effective immune response than were CD8 T cells, in contrast to the dominant focus on CD8 T cell responses in cancer

immunotherapy (Chen and Mellman, 2013; Topalian et al., 2015). Based on the assumption that CD8 T cells are the critical targets for therapy, numerous efforts focus on CD8 CAR T cells or identifying HLA class I epitopes that can be targeted with vaccines.

To address this question experimentally, we treated animals bearing MMTV-PyMT tumors with effective tumor-binding antibody therapy. During tumor rejection, we sacrificed animals, isolated the peripheral lymphoid organs (lymph nodes, spleen and blood), and sorted antigen-experienced (CD44+) CD4 and CD8 T cells. After expansion in culture, we transferred either the peripheral CD4 or CD8 T cell subsets into untreated animals bearing several large MMTV-PyMT tumors. While both CD4 and CD8 T cells were capable of mediating tumor rejection, animals receiving peripheral CD4 T cells experienced significantly more prolonged protection (Fig. 6C).

We then sought to identify the CD4 T cell subset responsible for orchestrating this anti-tumor activity. To investigate whether unique T cell phenotypes emerged after therapy, we performed an unsupervised clustering of all T cells across all tissues and visualized their similarities using a force-directed graph (Fig. 6D). Each tissue was colored uniquely, with light colors representing cells from the priming phase and dark colors representing cells from the rejection phase. Cells from animals left untreated or treated with ineffective therapy are colored black in Fig. 6D (with the inverted coloration in Fig. S7D).

T cells from the tumor microenvironment occupied markedly distinct regions of the graph, denoting that these cells exhibited unique characteristics from cells in other organs. In contrast, cells from the draining lymph node, spleen and blood were interspersed. Only animals treated with effective therapy contained T cells in the tumor similar to those from secondary lymphoid organs (Fig. 6D). CD4 T cells in the periphery were mixed together by tissue but distinctly organized by treatment (Fig. 6D). One region of the graph was highly enriched in cells from the periphery of mice receiving effective therapy (Fig 6E). The phenotype of these cells is most consistent with an activated, effector memory Th1 subset (CD44+CD69+CD62L-CD27^{low}T-bet+), and they uniquely expressed high levels of the immunoglobulin family member CD90 involved in T cell receptor signaling (Haeryfar and Hoskin, 2004). A similar subset also emerged after treatment in BP melanoma (Fig. 6F).

We then tested whether this subset of CD4 T cells found in the periphery conferred tumor protection. These cells were sorted from the periphery of treated MMTV-PyMT mice and transferred into untreated animals at the time of tumorigenesis following sublethal irradiation. Indeed, this subset of peripheral CD4 T cells was capable of conferring significant protection against tumor development (Fig. 6G). These results conclusively demonstrate that peripheral activated CD4 T cells are capable of orchestrating potent anti-tumor immunity.

A similar CD4 T cell subset is associated with a favorable response to immunotherapy in melanoma patients

We next determined whether similar CD4 T cells could be found in the blood of cancer patients who responded to immunotherapy. We recently described a clinical study of melanoma patients who received anti-CTLA-4 antibodies (Ipilimumab) in combination with

GM-CSF (Kwek et al., 2015). We analyzed blood from these patients both three and six weeks post-therapy using Statistical Scaffold. Consistent with our pre-clinical results, specific clusters of CD4 T cells were significantly elevated in responders compared to non-responders at both time points (Fig. 6H, Fig S6E). A subset of Tregs was also elevated in responders six weeks after therapy (Fig. S7E). The expanded clusters expressed lower levels of CD127 compared to the remaining CD4 T cells, indicative of activation, and lower levels of PD-1, suggesting that they were not exhausted (Fig. S7F). We confirmed these results by manually gating PD-1-CD127^{low} CD4 T cells (Fig. 6I). These results provide further experimental evidence of a critical role for CD4 T cells in coordinating effective anti-tumor immunity.

Simultaneous PD-L1 blockade breaks tolerance to un-injected tumors in multifocal disease

We next asked whether we could leverage this modeling-based approach to improve the efficacy of the tumor-binding antibody therapy. An observation from the initial analysis is that many immune cells in the tumor significantly upregulate PD-L1 after the effective therapy (Fig. 2B–C). PD-L1 is a repressor of T cell responses, and PD-L1 expression by tumor cells and immune cells mediates immunosuppression. We confirmed our observation by globally mapping cell subsets exhibiting significant differences in PD-L1 expression between therapies (Fig. 7A). In the effectively treated animals, all myeloid cell subsets and some T cell subsets upregulated PD-L1 after effective therapy, as did tumor cells (Fig. 7B). We hypothesized that PD-L1/PD-1 signaling may limit the efficacy of these immune responses. However, because these tumors do regress, a modified experimental setting was required to investigate this possibility.

MMTV-PyMT animals eventually develop tumors in all of their mammary fat pads. We had previously observed that, when animals were treated with tumor-binding antibody therapy after they had developed many tumors, only the injected tumor is rejected. In addition the injected tumor, we also observed PD-L1 upregulation in the draining lymph node and blood (Fig. 7C–D), as well as un-injected tumors during the priming phase (Fig. 7E–F). We hypothesized that the PD-L1/PD-1 axis may act more broadly to protect un-injected tumors.

We thus asked whether systemic administration of anti-PD-L1 blocking antibodies might break tolerance to un-injected tumors. We treated MMTV-PyMT animals once they had developed many tumors with tumor-binding antibody therapy alone or in combination with anti-PD-L1. Combination with anti-PD-L1 resulted in additional reduction in overall tumor burden (Fig. 7G) and rejection of multiple, un-injected tumors (Fig. 7H). These results suggest that the PD-L1/PD-1 axis dampens the anti-tumor immune response to distal tumors, despite the systemic nature of the immune response.

Discussion

The variance in clinical responses to immunotherapy suggests that productive immune responses against cancer are necessarily complex. There is an urgent need for methods to understand the nature of anti-tumor immunity to more reproducibly harness the immune system against cancer.

Here, we provide a systems-wide, organism-wide assessment of effective anti-tumor immune responses. Even for a therapy delivered intratumorally, a systemic immune response was required for tumor rejection. The effective tumor-binding antibody therapy activates a broad immune cell network including dendritic cells, which can prime T cells in the periphery. This could explain its efficacy against less immunogenic tumors compared to anti-PD-1, which is thought to act downstream on T cells themselves. With the increased use of immunotherapies, systemic responses should be taken into account when determining radiation or surgical regimens including lymphadenectomy.

Our results indicate that secondary lymphoid organs are critical sites of T cell generation. This contrasts with results from a B16 melanoma model engineered to express strong model antigens, where intratumoral T cells could mediate rejection when combination immunotherapy was initiated early after tumor implantation (Spranger et al., 2014). While most adoptive T cell protocols utilize tumor-infiltrating cells (Rosenberg, 2014), a recent study has shown that T cells from blood can be used successfully (Cohen et al., 2015). While immune cells in the microenvironment may be sufficient in some settings, development of new immunotherapies must consider the benefit of systemic immunity.

Many studies have focused on CD8 T cells (Chen and Mellman, 2013; Im et al., 2016), with less emphasis on harnessing CD4 T cells (Tran et al., 2014; Xie et al., 2010). In other contexts, CD4 T cells orchestrate functional immune responses by coordinating immune activity (Swain et al., 2012). Our results extend this notion to anti-tumor immunity, providing a rationale for leveraging CD4 T cell responses in cancer.

These results highlight the benefit of system-wide assessments. Simple prognostic metrics have been proposed for monitoring anti-tumor immunity, including Treg frequency in tumors (Bates et al., 2006; Curiel et al., 2004). Productive immunity in this setting was accompanied by an increase in Treg frequency and proliferation in the context of a powerful T cell response. With high throughput and high dimensional single-cell technologies such as mass cytometry, assessing all immune cells simultaneously is now achievable, enabling individual metrics to be contextualized into the broader immune state. For instance, the systemic proliferative response identified may provide a means for noninvasive monitoring during immunotherapy. The graphical user interface that accompanies Scaffold maps (https://github.com/nolanlab/scaffold/) enables further interrogation of this dataset. Using similar approaches, we expect that future studies will identify a multitude of drivers of effective responses.

A thorough understanding of the immune dynamics essential to any anti-tumor response requires comparison across numerous therapies. A systematic approach to understanding the mechanisms of new therapies will shed light on the core elements of immune activation required to reproducibly reject tumors. Additional behavioral programs, such as signaling, metabolism and cytokine production, would enrich our view of the immune response.

These approaches also enabled rational design of drug combinations. PD-L1 induction mediated active resistance before T cells primed in the periphery could reach distal tumors,

revealing another opportunity for modulating this pathway. System-wide studies should provide numerous opportunities for augmenting therapeutic efficacy.

The number of clinical trials in immunotherapy today provides opportunities to perform parallel studies in humans, building on our initial analysis here. A systematic understanding of anti-tumor immunity at the organismal and systems levels should enable significant progress in developing rational immunotherapeutic strategies.

STAR Methods

CONTACT FOR REAGENT AND RESOURCE SHARING

Further information and requests for resources and reagents should be directed to and will be fulfilled by lead contact Matthew Spitzer (matthew.spitzer@ucsf.edu).

EXPERIMENTAL MODEL AND SUBJECT DETAILS

Animals

Female MMTV-PyMT mice and male Tyr::CreER; $Braf^{V600E/+}$; $Pten^{lox/lox}$ mice were bred in our colony at Stanford University. All mice were housed in an American Association for the Accreditation of Laboratory Animal Care–accredited animal facility and maintained in specific pathogen-free conditions. Animal experiments were approved and conducted in accordance with Stanford University Asia Pacific Laboratory Accreditation Cooperation #13605. Animals began treatment when they developed a primary tumor reaching $25mm^2$ in area (referred to as day 0) and were randomized to different treatment groups. Wild-type female FVB, BALB/c or C57BL/6 mice were purchased from The Jackson Laboratory and housed at our facility or were bred at Stanford University. Mice were transplanted with 2.5×10^5 tumor cells when the mice were nine to twelve weeks of age. 4T1 breast cancer cells were transplanted into the fourth mammary fat pad, and MC38 cells were transplanted into the subcutaneous region of the flank when animals were between 8–10 weeks old. Animals were housed under standard SPF conditions with typical light/dark cycles and standard chow.

Human Subjects

Eligible patients were adults with histologically confirmed unresectable metastatic melanoma as previously reported (Kwek et al., 2015). The protocol was approved by the Institutional Review Board of each participating institution and was conducted in accordance with the ethical principles of the Declaration of Helsinki and within the Good Clinical Practice guidelines as defined by the International Conference on Harmonization. All patients gave written informed consent for participation in the study. The trial was registered on ClinicalTrials.gov with Identifier NCT01363206.

At the initiation of treatment (months 1–3), patients were treated with four cycles of GM-CSF and ipilimumab administered every 3 weeks. Ipilimumab was administered intravenously at a dose of 10 mg/kg on day 1 of each 21 d cycle. GM-CSF was administered subcutaneously daily for 14 d at a dose of $125\ mg/m^2$ beginning on day 1 of each cycle. After the first four cycles of treatment, GM-CSF administration without ipilimumab

continued for four more cycles on the same schedule and dose for the first 14 d of every 21 d cycle until month 6. Maintenance therapy began at month 6 and consisted of ipilimumab in the same dose (10 mg/kg) combined with 14 d of GM-CSF. This combination was administered every 3 mo thereafter for up to 2 y or until disease progression or unacceptable toxicity. Blood samples were obtained at week 3 (end of cycle 1) and at week 6 (end of cycle 2) and were cryopreserved for subsequent analysis by flow cytometry.

Cell Lines

4T1 cells were purchased from the ATCC (catalog number CRL-2539). 4T1 and MC38 cells were cultured in RPMI-1640 supplemented with 10% FCS, 2 mM L-glutamine,100 U/mL penicillin and 100 μg/mL penicillin/streptomycin.

Primary Cell Cultures

MMTV-PyMT T Cell Transfer Studies—MMTV-PyMT animals bearing 25mm^2 tumors were treated with anti-CD40, IFNγ, and allogeneic (CD-1) IgG antibodies as described under “Treatments”. On day 7 following treatment, mice were euthanized and their spleens and lymph nodes harvested. Following tissue dissociation, T cells were enriched using the EasySep Mouse T Cell Enrichment Kit (StemCell, 588CAD), and sorted by FACS for the following markers: CD4+CD69+CD44+Lin- or CD8a+Ly6C+CD44+Lin−. Cells were expanded in vitro by culturing in RPMI-1640 supplemented with 10% FCS, 2 mM L-glutamine,100 U/mL penicillin, 100 μg/mL penicillin/streptomycin, 30IU of hIL-2 and anti-CD3/CD28 Dynabeads (Life Technologies, 11452D) at a bead:cell ratio of 1:2. Cells were expended with beads for 7 days, after which the beads were removed and the cells were cultured for an additional two days. Tumor-bearing naïve MMTV-PyMT recipient mice were sub-lethally irradiated with 4 Gray. Subsequently, 3×10^6 CD4 or CD8 T cell populations were transferred to the mice through tail vein injections in 200μL of PBS. Tumor burden was assessed on days 0, 4, 8, 12, and 16 following T cell transfer.

METHOD DETAILS

Tumor-Binding Antibody Purification

Mouse antibodies were obtained from the pooled sera of retired breeders from Charles River using protein-G columns (GE Healthcare). The levels of purified IgG and were measured using a NanoDrop spectrophotometer (Thermo Scientific). The capacity of purified antibodies to bind tumor cells was tested by flow cytometry before their use *in vivo*.

Treatments

Animals treated for tumor kinetics analysis were injected intratumorally with 100μg anti-CD40 (clone FGK4.5; BioXCell) and 1μg IFNγ (Biolegend) with or without 300μg B6 IgG antibodies and 300μg CD-1 IgG antibodies. Animals treated for mass cytometry analysis with tumor-binding antibody therapy were injected intratumorally with 400μg allo-IgG (either B6 or CD-1) and 100μg anti-CD40 and IFNγ or with 250μg anti-PD-1 (clone RMP1-14, BioXCell) injected i.p. Injections were performed on day 0 and day 2. In some cases, mice were injected i.p. with 200 μg of anti-PD-L1 (clone 10F.9G2; BioXCell) every 3 days until the experiment was terminated. Day 0 was considered the first day of treatment.

Mass Cytometry Antibodies

A summary of all mass cytometry antibodies, reporter isotopes and concentrations used for analysis can be found in Supplementary Table 1. Primary conjugates of mass cytometry antibodies were prepared using the MaxPAR antibody conjugation kit (Fluidigm) according to the manufacturer's recommended protocol. Following labeling, antibodies were diluted in Candor PBS Antibody Stabilization solution (Candor Bioscience GmbH, Wangen, Germany) supplemented with 0.02% NaN_3 to between 0.1 and 0.3 mg/mL and stored long-term at 4°C. Each antibody clone and lot was titrated to optimal staining concentrations using primary murine samples. One antibody cocktail was prepared for the staining of all samples for mass cytometry analysis.

Cell Preparation

All tissue preparations were performed simultaneously from each individual mouse. After euthanasia by $C0_2$ inhalation, peripheral blood was collected via the posterior vena cava prior to perfusion of the animal and transferred into sodium heparin-coated vacuum tubes prior to 1:1 dilution in RMPI 1640. Spleens and lymph nodes were homogenized in PBS + 5mM EDTA at 4°C. Bone marrow was flushed from femuri and resuspended in PBS + 5mM EDTA at 4°. Tumors were finely minced and digested in RPMI 1640 with 1 mg/ml collagenase IV, and 0.1 mg/ml DNase I. After digestion, cells re-suspended cells were quenched with RPMI with 10% FCS at 4°C. Cells were then homogenized in RPMI with 10% FCS. All tissues except peripheral blood were washed with PBS with 5mM EDTA and resuspended 1:1 with PBS with 5mM EDTA and 100μM Ciaplatin (Enzo Life Sciences, Farmingdale, NY) for 60s before quenching 1:1 with PBS with 0.5% BSA and 5mM EDTA to determine viability as previously described (Spitzer et al., 2015). Cells were centrifuged at 500g for 5 min at 4°C and resuspended in PBS with 0.5% BSA and 5mM EDTA at a density between $1–10*10^6$ cells/ml. Suspensions and blood were fixed for 10 min at RT using 1:1.4 Proteomic Stabilizer according to the manufacturer's instructions (Smart Tube Inc., Palo Alto, CA) and frozen at −80°C.

Mass-Tag Cellular Barcoding

Mass-tag cellular barcoding was preformed as previously described (Zunder et al., 2015). Briefly, $1*10^6$ cells from each animal were barcoded with distinct combinations of stable Pd isotopes chelated by isothiocyanobenzyl-EDTA in 0.02% saponin in PBS. Samples from any given tissue from one mouse per treatment group were barcoded together, with at least 3 biological replicates per treatment group across different plates. Cells were washed two times in PBS with 0.5% BSA and 0.02% NaN3 and pooled into a single FACS tube (BD Biosciences). After data collection, each condition was deconvoluted using a single-cell debarcoding algorithm (Zunder et al., 2015).

Mass Cytometry Staining and Measurement

Cells were resuspended in PBS with 0.5% BSA and 0.02% NaN_3 and metal-labeled antibodies against CD16/32 were added at 20μg/ml for 5 min at RT on a shaker to block Fc receptors. Surface marker antibodies were then added, yielding 500 uL final reaction volumes and stained at room temperature for 30min at RT on a shaker. Following staining,

cells were washed 2 more times with PBS with 0.5% BSA and 0.02% NaN3 then permeabilized with 4°C methanol for at 10 min at 4°C. Cells were then wash ed twice in PBS with 0.5% BSA and 0.02% NaN_3 to remove remaining methanol, and then stained with intracellular antibodies in 500 μL for 30 min at RT on a shaker. Cells were washed twice in PBS with 0.5% BSA and 0.02% NaN_3 and then stained with 1 mL of 1:4000 191/193Ir DNA intercalator (Fluidigm) diluted in PBS with 1.6% PFA overnight. Cells were then washed once with PBS with 0.5% BSA and 0.02% NaN_3 and then two times with double-deionized (dd)H20. Care was taken to assure buffers preceding analysis were not contaminated with metals in the mass range above 100 Da. Mass cytometry samples were diluted in ddH2O containing bead standards (see below) to approximately 106 cells per mL and then analyzed on a CyTOF^{TM} 2 mass cytometer (Fluidigm) equilibrated with ddH_2O. We analyzed 1–5*10^5 cells per animal, per tissue, per time point, per treatment, consistent with generally accepted practices in the field.

Bead Standard Data Normalization

Just before analysis, the stained and intercalated cell pellet was resuspended in ddH_2O containing the bead standard at a concentration ranging between 1 and 2*10^4 beads per ml as previously described (Finck et al., 2013). The bead standards were prepared immediately before analysis, and the mixture of beads and cells were filtered through a filter cap FACS tubes (BD Biosciences) before analysis. All mass cytometry files were normalized together using the mass cytometry data normalization algorithm (Finck et al., 2013), which uses the intensity values of a sliding window of these bead standards to correct for instrument fluctuations over time and between samples.

Scaffold Map Generation

Total live leukocytes (excluding erythrocytes) were used for all analyses. Cells from each tissue for all animals were clustered together (rather than performing CLARA clustering on each file individually as originally implemented in Spitzer et al., *Science*, 2015.) Cells were then deconvolved into their respective samples. Cluster frequencies or the Boolean expression of Ki67 or PD-L1 for each cluster were passed into the Significance Across Microarrays algorithm (Bair and Tibshirani, 2004; Bruggner et al., 2014), and results were tabulated into the Scaffold map files for visualization through the graphical user interface. Cluster frequencies were calculated as a percent of total live nucleated cells (excluding erythrocytes). For each cluster in each tissue, the most similar cluster in every other tissue is included as Table S3 for comparisons.

Scaffold maps were then generated as previously reported (Spitzer et al., 2015). Briefly, we chose the spleen data to spatialize the initial Scaffold map because all major, mature immune cell populations are present in that tissue. A graph was constructed by first connecting together the nodes representing the manually gated landmark populations and then connecting to them the nodes representing the cell clusters as well as connecting the clusters to one another. Each node is associated with a vector containing the median marker values of the cells in the cluster (unsupervised nodes) or gated populations (landmark nodes). Edge weights were defined as the cosine similarity between these vectors after comparing the results from the implementation of several distance metrics. Edges of low weight were

filtered out. We experimented with different threshold values for the weights and we found values of 0.8 for the initial subgraph of landmark nodes, and 0.7 for the complete graph to produce satisfying results. The graph was then laid out using an in-house R implementation of the ForceAtlas2 algorithm from the graph visualization software Gephi. To overlay the additional samples on the spleen map, the position and identity of the landmark nodes was fixed and the clusters of each sample were connected to the landmark nodes as described above. Once again the graphs were laid out using ForceAtlas2 but this time only the unsupervised nodes were allowed to move. All analyses were performed using the open source Scaffold maps R package available at github.com/nolanlab/scaffold.

Cell Population Expression Profiles

Cell clusters of interest were further investigated by visualizing the distribution of protein expression within the cells comprising each cluster as a histogram. This was performed using the density visualization feature of the Scaffold maps R package. Histograms shown in the figures were created by exporting clusters as .FCS files using the Scaffold maps R package and using the flowCore and ggplot2 packages in R to write vector histogram plots. Scripts are available at github.com/mhspitzer.

Unsupervised Force-Directed Graph Generation

Cells were manually gated as Live CD45+ lineage- (Ter119, Ly6G, Siglec-F, CD19, B220, F4/80, CD11c, PDCA-1, FcεR1α) and then CD3+ to identify T cells. The gated cell populations for each tissue/timepoint/treatment group were clustered independently in 50 clusters using clara in R. The clusters for all the tissues were combined in a single graph with edge weights defined as the cosine similarity between the vectors of median marker values of each cluster. All the pairwise distances were calculated and for each node only the 10 edges of highest weight were retained. The graph was then laid out using the ForceAtlas2 algorithm in Gephi (https://gephi.org).

Correlation Network Analysis and Connectivity Analysis

Immune cell subsets were gated from mass cytometry data, and the frequency of each subset in each tissue of each mouse was calculated. For animals receiving effective therapy or those receiving no or ineffective therapy, pairwise Spearman correlations were calculated for each immune cell subset, and hierarchical clustering was performed to organize the correlation matrix. The hierarchical clustering result from the mice receiving effective therapy was additionally imposed on the correlation matrix for the animals receiving no or ineffective therapy as a means of comparing the networks.

For the connectivity analysis, an adjacency matrix was created from the correlation matrix of animals receiving effective therapy, using a Spearman correlation coefficient of 0.5 as the threshold. The number of remaining correlations was tabulated for each immune cell population from each tissue, and these were rank ordered. The graph of the adjacency matrix visualizes all positive and negative correlations present in the adjacency matrix for each subset.

Histology and Immunohistochemistry

Following excision from mice, tissues were fixed in 4% buffered formalin for one hour at room temperature. Tissues were then transferred to 30% sucrose solution in PBS and left overnight at 4°C. They were then embedded in O.C.T. Compound (Tissue-Tek) and frozen on dry ice. Tissue blocks were sectioned at 6μm on a microtome onto positively charged glass slides (Fisher Scientific) and stained with Hematoxylin and Eosin (H&E) according to standard protocols.

Additional slides were blocked with PBS containing 10% normal goat serum and 5% BSA for 30 min at room temperature and stained for the following antigens at a 1:100 dilution overnight at 4°C: CD45 (30-F11, BioLegend), CD8 α (53–6.7, BioLegend), CD4 (RM4-5, BioLegend), and CD11b (M1/70, BioLegend), mounted with LabVision PermaFluor Aqueous Mounting Medium (Thermo Scientific), and imaged on a Zeiss LSM700 confocal microscope. When co-stained with TUNEL, sections were stained overnight at 4°C with 1:50 dilution of rat-anti mouse polyoma virus- middle T antigen (Santa Cruz Biotechnology). Sections were then washed three times in PBS, incubated for 1 hour at room temperature with, and stained with 1:100 Alexa Fluor 647-conjugated anti-CD8β (YTS156.7.7) and with 1:200 Alexa Fluor 488-Conjugated anti-rat IgG antibodies (BioLegend). Terminal deoxynucleotidyl transferase–mediated dUTP nick end labeling (TUNEL) assays were performed according to manufacturer's instructions (Roche manual). Briefly, cells were washed thrice in PBS, and fixed in freshly prepared 4% paraformaldehyde in PBS for 1 h at room temperature, and then washed with PBS and permeabilized in 0.1% Triton X-100 in 0.1% sodium citrate. Cells were then incubated with TUNEL reaction mixture (Roche) for 60 min at 37°C i n a humidified atmosphere in the dark.

Leukocyte Egress Blockade

Animals bearing 25mm^2 tumors were treated with alloIgG (from B6 mice), anti-CD40 and IFNγ and were randomized to receive daily i.p. injections of FTY720 (3 mg/kg) or ethanol control beginning one day prior to therapy.

Adoptive T Cell Transfer

Balb/c mice were injected orthotopically into the fourth mammary fat pad with 10^5 4T1 tumor cells. On days 12 and 14, mice were injected intratumorally with 100μg anti-CD40 (clone FGK4.5; BioXCell) and 1μg IFNγ (Biolegend) and 400μg allo-IgG along with daily i.p. injections of FTY720 (3mg/kg). On day seven, mice were euthanized and the draining lymph nodes and spleens were removed and mechanically dissociated to obtain single cell suspension. T cells were then enriched by negative selection using magnetic beads (EasySep, StemCell technologies) and a total of 8×10^6 cells were injected intravenously into Balb/c female mice. After one day, both T cell-recipient mice and naïve control mice were challenged with 5×10^4 4T1 tumor cells subcutaneously. Starting the day of T cell transfer, mice were treated twice a day for five days with 220,000 IU of human IL-2 (Peprotech).

Flow Cytometry

For human samples, cell surface staining was performed in fluorescence-activated cell sorting (FACS) buffer for 30 min at 4°C. Intracellular foxhead box P3 (FoxP3) was performed using the FoxP3 fix/perm buffer set (Biolegend, Inc.) according to the manufacturer's protocol. The following anti-human antibodies were used: (Alexa Fluor 700)-CD3 (clone HIT3a), (Brilliant violet 570)-CD4 (clone RPA-T4), (Brilliant violet 650)-CD25 (clone BC96), (Alexa Fluor 647)-CD127 (clone A019D5), (Alexa Fluor 488)-FoxP3 (clone 206D), and (Brilliant violet 421)-PD-1 (clone EH12.2H7). All antibodies were purchased from Biolegend, Inc. Stained cells were fixed with Fluorofix buffer (Biolegend, Inc.) according to manufacturer's instructions and analyzed with an LSR II flow cytometer (BD Biosciences).

QUANTIFICATION AND STATICAL ANALYSIS

Comparison of cell frequencies and protein expression in Statistical Scaffold was performed using Significance Analysis of Microarrays as described above and in Bair and Tibshirani, 2004 and Bruggner et al., 2014. Individual comparisons presented as stand alone panels were made using heteroskedastic, two-tailed t-tests performed in R.

Analysis of tumor sizes was performed by calculating a fold change in the size of the tumor at time point t compared to the baseline size at the time of treatment or adoptive transfer. Comparisons were made using heteroskedastic, two-tailed t-tests performed in R.

Frequency of human CD4+PD-1-CD127^{low} T cells (identified manually) was calculated as a percent of total leukocytes, and results were compared between responding and non-responding patients by two-tailed Wilcoxon rank-sum test performed in R.

DATA AND SOFTWARE AVAILABILITY

Statistical Scaffold and all mass cytometry data are publicly available at http://www.github.com/spitzerlab/Modeling_Effective_Cancer_Immunotherapy

Supplementary Material

Refer to Web version on PubMed Central for supplementary material.

Acknowledgments

We thank G.K. Fragiadakis and L.E. Sanman for helpful conversations and feedback and A. Trejo and A. Jager for CyTOF maintenance. M.H.S., P.F.G., L.F. and G.P.N. are investigators of the Parker Institute for Cancer Immunotherapy. G.P.N. has a personal financial interest in, and S.C.B. has been a paid consultant for Fluidigm, manufacturer of the mass cytometer utilized. E.G.E. is a founder and board member of Bolt Biotherapeutics, licensee of the alloIgG therapy. This work was supported by NIH F31CA189331 and DP5OD023056 to M.H.S.; F32CA189408 to N.R.F.; NIH U19AI057229, U19AI100627, R33CA183654, R01HL120724, DOD OC110674 and 11491122, Gates Foundation OPP1113682, NIAID HHSN272201200028C, FDA HHSF223201210194C BAA-12-00118 to G.P.N.; NIH R01CA196657 to G.P.N., E.G.E.; R01AI118884 to E.G.E.

References

Bair E, Tibshirani R. Semi-supervised methods to predict patient survival from gene expression data. PLoS Biol. 2004; 2:e108. [PubMed: 15094809]

Bandura DR, Baranov VI, Ornatsky OI, Antonov A, Kinach R, Lou X, Pavlov S, Vorobiev S, Dick JE, Tanner SD. Mass cytometry: technique for real time single cell multitarget immunoassay based on inductively coupled plasma time-of-flight mass spectrometry. Anal Chem. 2009; 81:6813–6822. [PubMed: 19601617]

Bates GJ, Fox SB, Han C, Leek RD, Garcia JF, Harris AL, Banham AH. Quantification of regulatory T cells enables the identification of high-risk breast cancer patients and those at risk of late relapse. J Clin Oncol. 2006; 24:5373–5380. [PubMed: 17135638]

Bendall SC, Bendall SC, Simonds EF, Simonds EF, Qiu P, Qiu P, Amir EAD, Amir EAD, Krutzik PO, Krutzik PO, et al. Single-Cell Mass Cytometry of Differential Immune and Drug Responses Across a Human Hematopoietic Continuum. Science. 2011; 332:687–696. [PubMed: 21551058]

Bos PD, Plitas G, Rudra D, Lee SY, Rudensky AY. Transient regulatory T cell ablation deters oncogene-driven breast cancer and enhances radiotherapy. J Exp Med. 2013; 210:2435–2466. [PubMed: 24127486]

Broz ML, Binnewies M, Boldajipour B, Nelson AE, Pollack JL, Erle DJ, Barczak A, Rosenblum MD, Daud A, Barber DL, et al. Dissecting the Tumor Myeloid Compartment Reveals Rare Activating Antigen-Presenting Cells Critical for T Cell Immunity. Cancer Cell. 2014:1–15.

Bruggner RV, Bodenmiller B, Dill DL, Tibshirani RJ, Nolan GP. Automated identification of stratifying signatures in cellular subpopulations. Proc Natl Acad Sci USa. 2014; 111:E2770–E2777. [PubMed: 24979804]

Bulliard Y, Jolicoeur R, Windman M, Rue SM, Ettenberg S, Knee DA, Wilson NS, Dranoff G, Brogdon JL. Activating Fc receptors contribute to the antitumor activities of immunoregulatory receptor-targeting antibodies. J Exp Med. 2013; 210:1685–1693. [PubMed: 23897982]

Carmi Y, Spitzer MH, Linde IL, Burt BM, Prestwood TR, Perlman N, Davidson MG, Kenkel JA, Segal E, Pusapati GV, et al. Allogeneic IgG combined with dendritic cell stimuli induce antitumour T-cell immunity. Nature. 2015:1–6.

Chen DS, Mellman I. Oncology meets immunology: the cancer-immunity cycle. Immunity. 2013; 39:1–10. [PubMed: 23890059]

Cheng G, Yuan X, Tsai MS, Podack ER, Yu A, Malek TR. IL-2 receptor signaling is essential for the development of Klrg1+ terminally differentiated T regulatory cells. J Immunol. 2012; 189:1780–1791. [PubMed: 22786769]

Cohen CJ, Gartner JJ, Horovitz-Fried M, Shamalov K, Trebska-McGowan K, Bliskovsky VV, Parkhurst MR, Ankri C, Prickett TD, Crystal JS, et al. Isolation of neoantigen-specific T cells from tumor and peripheral lymphocytes. J Clin Invest. 2015; 125:3981–3991. [PubMed: 26389673]

Coley WB. The treatment of malignant tumors by repeated inoculations of erysipelas: with a report of ten original cases. Am J Med Sci. 1893:487–511.

Curiel TJ, Coukos G, Zou L, Alvarez X, Cheng P, Mottram P, Evdemon-Hogan M, Conejo-Garcia JR, Zhang L, Burow M, et al. Specific recruitment of regulatory T cells in ovarian carcinoma fosters immune privilege and predicts reduced survival. Nat Med. 2004; 10:942–949. [PubMed: 15322536]

Dankort D, Curley DP, Cartlidge RA, Nelson B, Karnezis AN, Damsky WE Jr, You MJ, DePinho RA, McMahon M, Bosenberg M. BrafV600E cooperates with Pten loss to induce metastatic melanoma. Nat Genet. 2009; 41:544–552. [PubMed: 19282848]

Finck R, Simonds EF, Jager A, Krishnaswamy S, Sachs K, Fantl W, Pe'er D, Nolan GP, Bendall SC. Normalization of mass cytometry data with bead standards. Cytometry A. 2013; 83:483–494. [PubMed: 23512433]

Gabrilovich DI, Ostrand-Rosenberg S, Bronte V. Coordinated regulation of myeloid cells by tumours. Nature Reviews Immunology. 2012; 12:253–268.

Haeryfar SMM, Hoskin DW. Thy-1: More than a Mouse Pan-T Cell Marker. The Journal of Immunology. 2004; 173:3581–3588. [PubMed: 15356100]

Hänninen A, Maksimow M, Alam C, Morgan DJ, Jalkanen S. Ly6C supports preferential homing of central memory CD8+ T cells into lymph nodes. Eur J Immunol. 2011; 41:634–644. [PubMed: 21308682]

Herbst RS, Soria JC, Kowanetz M, Fine GD, Hamid O, Gordon MS, Sosman JA, McDermott DF, Powderly JD, Gettinger SN, et al. Predictive correlates of response to the anti-PD-L1 antibody MPDL3280A in cancer patients. Nature. 2014; 515:563–567. [PubMed: 25428504]

Hotson D, Gopinath S, Nolan GP, Monack DM. A systems biology approach to persistent Salmonella infection reveals a neutrophil dependent IL-2 mediated dampening of TH1 response. 2012:1–29.

Ideker T, Krogan NJ. Differential network biology. Mol Syst Biol. 2012; 8:1–9.

Im SJ, Hashimoto M, Gerner MY, Lee J, Kissick HT, Burger MC, Shan Q, Hale JS, Lee J, Nasti TH, et al. Defining CD8+ T cells that provide the proliferative burst after PD-1 therapy. Nature. 2016:1–20.

Jiang Y, Li Y, Zhu B. T-cell exhaustion in the tumor microenvironment. Cell Death Dis. 2015; 6:e1792. [PubMed: 26086965]

Kantoff PW, Higano CS, Shore ND, Berger ER, Small EJ, Penson DF, Redfern CH, Ferrari AC, Dreicer R, Sims RB, et al. Sipuleucel-T immunotherapy for castration-resistant prostate cancer. N Engl J Med. 2010; 363:411–422. [PubMed: 20818862]

Kvistborg P, Philips D, Kelderman S, Hageman L, Ottensmeier C, Joseph-Pietras D, Welters MJP, van der Burg S, Kapiteijn E, Michielin O, et al. Anti-CTLA-4 therapy broadens the melanoma-reactive CD8+ T cell response. Science Translational Medicine. 2014; 6:254ra128–254ra128.

Kwek SS, Kahn J, Greaney SK, Lewis J, Cha E, Zhang L, Weber RW, Leonard L, Markovic SN, Fong L, et al. GM-CSF and ipilimumab therapy in metastatic melanoma: Clinical outcomes and immunologic responses. Oncoimmunology. 2015; 5:e1101204–e1101211. [PubMed: 27141383]

Matloubian M, Lo CG, Cinamon G, Lesneski MJ, Xu Y, Brinkmann V, Allende ML, Proia RL, Cyster JG. Lymphocyte egress from thymus and peripheral lymphoid organs is dependent on S1P receptor 1. Nature. 2004; 427:355–360. [PubMed: 14737169]

Pelletier N, McHeyzer-Williams LJ, Wong KA, Urich E, Fazilleau N, McHeyzer-Williams MG. Plasma cells negatively regulate the follicular helper T cell program. Nature Immunology. 2010; 11:1110–1118. [PubMed: 21037578]

Porter DL, Levine BL, Kalos M, Bagg A, June CH. Chimeric Antigen Receptor–Modified T Cells in Chronic Lymphoid Leukemia. N Engl J Med. 2011; 365:725–733. [PubMed: 21830940]

Restifo NP, Dudley ME, Rosenberg SA. Adoptive immunotherapy for cancer: harnessing the T cell response. Nature Reviews Immunology. 2012; 12:269–281.

Rosenberg SA. Decade in review—cancer immunotherapy: Entering the mainstream of cancer treatment. Nat Rev Clin Oncol. 2014; 11:630–632. [PubMed: 25311350]

Simpson TR, Li F, Montalvo-Ortiz W, Sepulveda MA, Bergerhoff K, Arce F, Roddie C, Henry JY, Yagita H, Wolchok JD, et al. Fc-dependent depletion of tumor-infiltrating regulatory T cells co-defines the efficacy of anti-CTLA-4 therapy against melanoma. J Exp Med. 2013; 210:1695–1710. [PubMed: 23897981]

Spitzer MH, Gherardini PF, Fragiadakis GK, Bhattacharya N, Yuan RT, Hotson AN, Finck R, Carmi Y, Zunder ER, Fantl WJ, et al. An interactive reference framework for modeling a dynamic immune system. Science. 2015; 349:1259425–1259425. [PubMed: 26160952]

Spranger S, Koblish HK, Horton B, Scherle PA, Newton R, Gajewski TF. Mechanism of tumor rejection with doublets of CTLA-4, PD-1/PD-L1, or IDO blockade involves restored IL-2 production and proliferation of CD8(+) T cells directly within the tumor microenvironment. Journal for ImmunoTherapy of Cancer. 2014; 2:3. [PubMed: 24829760]

Swain SL, McKinstry KK, Strutt TM. Expanding roles for CD4+ T cells in immunity to viruses. Nature Reviews Immunology. 2012; 12:136–148.

Topalian SL, Drake CG, Pardoll DM. Immune Checkpoint Blockade: A Common Denominator Approach to Cancer Therapy. Cancer Cell. 2015; 27:450–461. [PubMed: 25858804]

Tran E, Turcotte S, Gros A, Robbins PF, Lu YC, Dudley ME, Wunderlich JR, Somerville RP, Hogan K, Hinrichs CS, et al. Cancer immunotherapy based on mutation-specific CD4+ T cells in a patient with epithelial cancer. Science. 2014; 344:641–645. [PubMed: 24812403]

Wherry EJ, Ha SJ, Kaech SM, Haining WN, Sarkar S, Kalia V, Subramaniam S, Blattman JN, Barber DL, Ahmed R. Molecular Signature of CD8+ T Cell Exhaustion during Chronic Viral Infection. Immunity. 2007; 27:670–684. [PubMed: 17950003]

Xie Y, Akpinarli A, Maris C, Hipkiss EL, Lane M, Kwon EKM, Muranski P, Restifo NP, Antony PA. Naive tumor-specific CD4 +T cells differentiated in vivo eradicate established melanoma. Journal of Experimental Medicine. 2010; 207:651–667. [PubMed: 20156973]

Zunder ER, Finck R, Behbehani GK, Amir EAD, Krishnaswamy S, Gonzalez VD, Lorang CG, Bjornson Z, Spitzer MH, Bodenmiller B, et al. Palladium-based mass tag cell barcoding with a doublet-filtering scheme and single-cell deconvolution algorithm. Nat Protoc. 2015; 10:316–333. [PubMed: 25612231]

Highlights

- System-wide models reveal coordinated anti-tumor immunity across the organism
- Tumor eradication requires immune activation in the periphery
- Network analysis identifies CD4 T cells sufficient to initiate immune responses
- PD-L1 upregulation early post-therapy protects distal tumors from systemic immunity

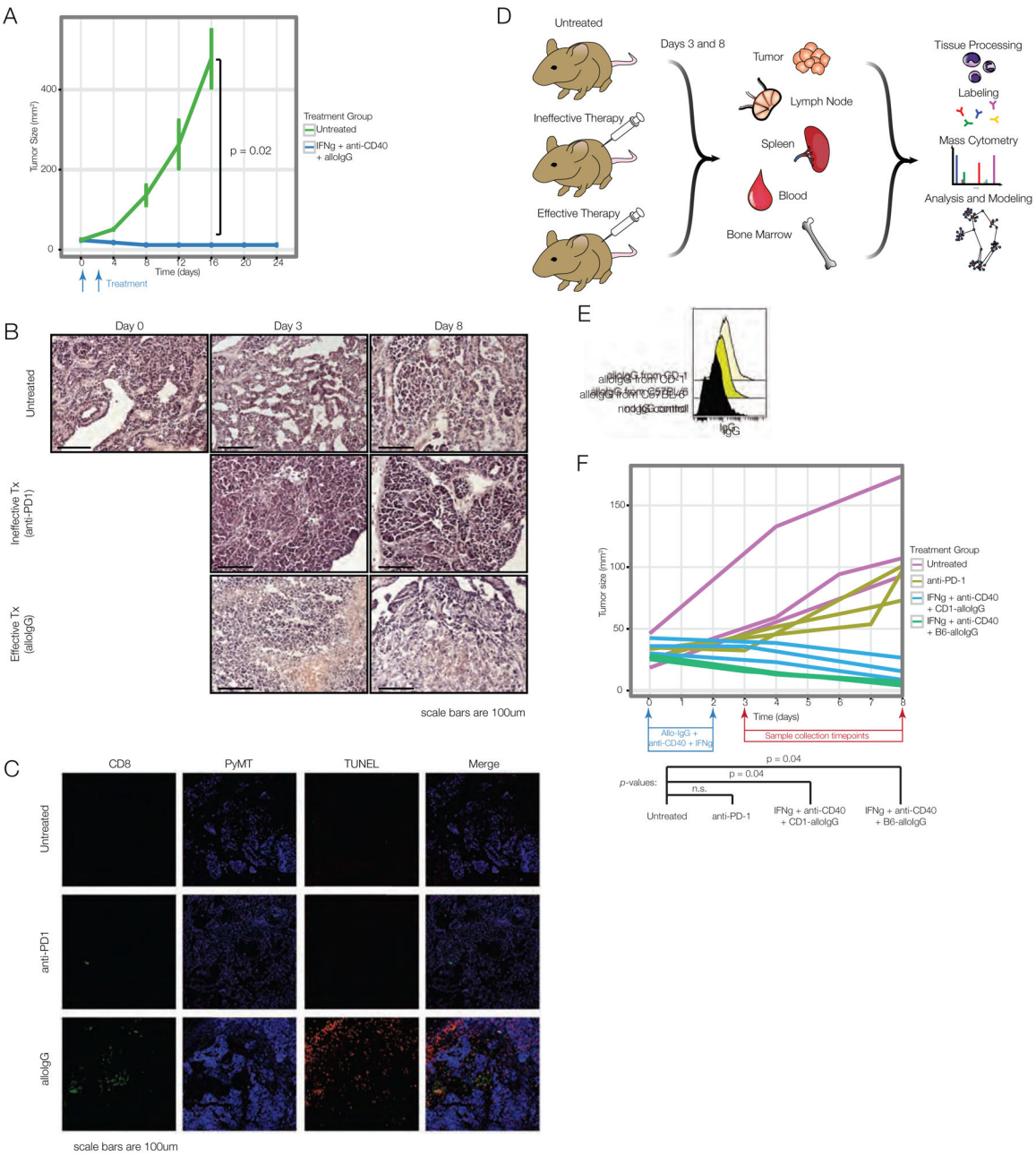

Figure 1. Tumor-binding antibodies and dendritic cell adjuvants induce rejection of spontaneous breast tumors

(A) MMTV-PyMT mice with tumors of 25mm^2 treated with allogeneic IgG pooled from C57BL/6 and CD-1 mice, anti-CD40 and IFNγ or untreated. (B) H&E and (C) immunofluorescence of tumors from treated mice 8 days after therapy. (D) Mass cytometry experiment. (E) Binding of IgG antibodies from naïve CD-1 or C57BL/6 mice to MMTV-PyMT tumor cells. (F) Tumor sizes, day 8 after therapy, for mass cytometry. See also Fig. S1, Table S1.

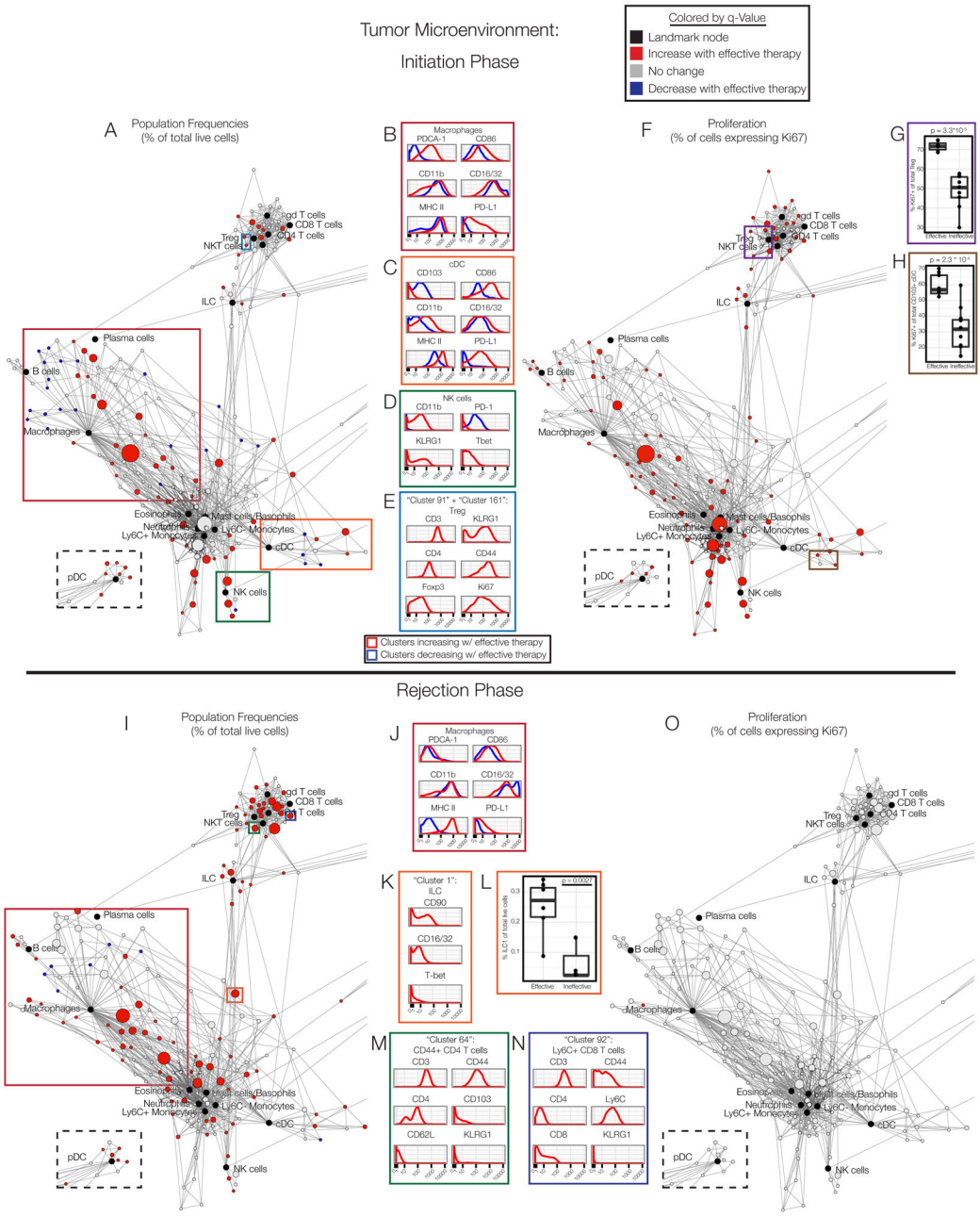

Figure 2. The tumor microenvironment is remodeled and immune cells transiently proliferate during effective responses

(A) Statistical Scaffold map of the tumor on day 3. Black nodes are Landmark nodes, representing canonical cell populations identified manually. Other nodes reflect unsupervised clustering of live leukocytes (see Methods). Clusters in red denote populations significantly higher in frequency with effective therapy; blue clusters are significantly lower in frequency. pDC are in the dashed box to maximize space. Colored boxes are populations analyzed in B–E. (B) Expression profile of B cell, (C) cDC, (D) NK cell, or (E) Treg cell clusters expanding with effective therapy (red) versus those decreasing (blue). (F) Scaffold map of Ki67 expression in immune cells in the tumor on day 3. Subsets more proliferative

after effective therapy in red. (G) Percent of Ki67+ Treg. (H) Percent of Ki67+ cDC. (I) Scaffold map of the tumor on day 8. (J) Expression profile of macrophage clusters expanding with effective therapy (red) versus those decreasing (blue). (K) Expression profile of ILC cluster increasing with effective therapy. (L) ILC1 frequencies. (M) Expression profile of CD4 T cell or (N) CD8 T cell cluster increasing with effective therapy. (O) Scaffold map of Ki67 expression in immune cells in the tumor on day 8. See also Fig. S2–S4, Tables S2–S3.

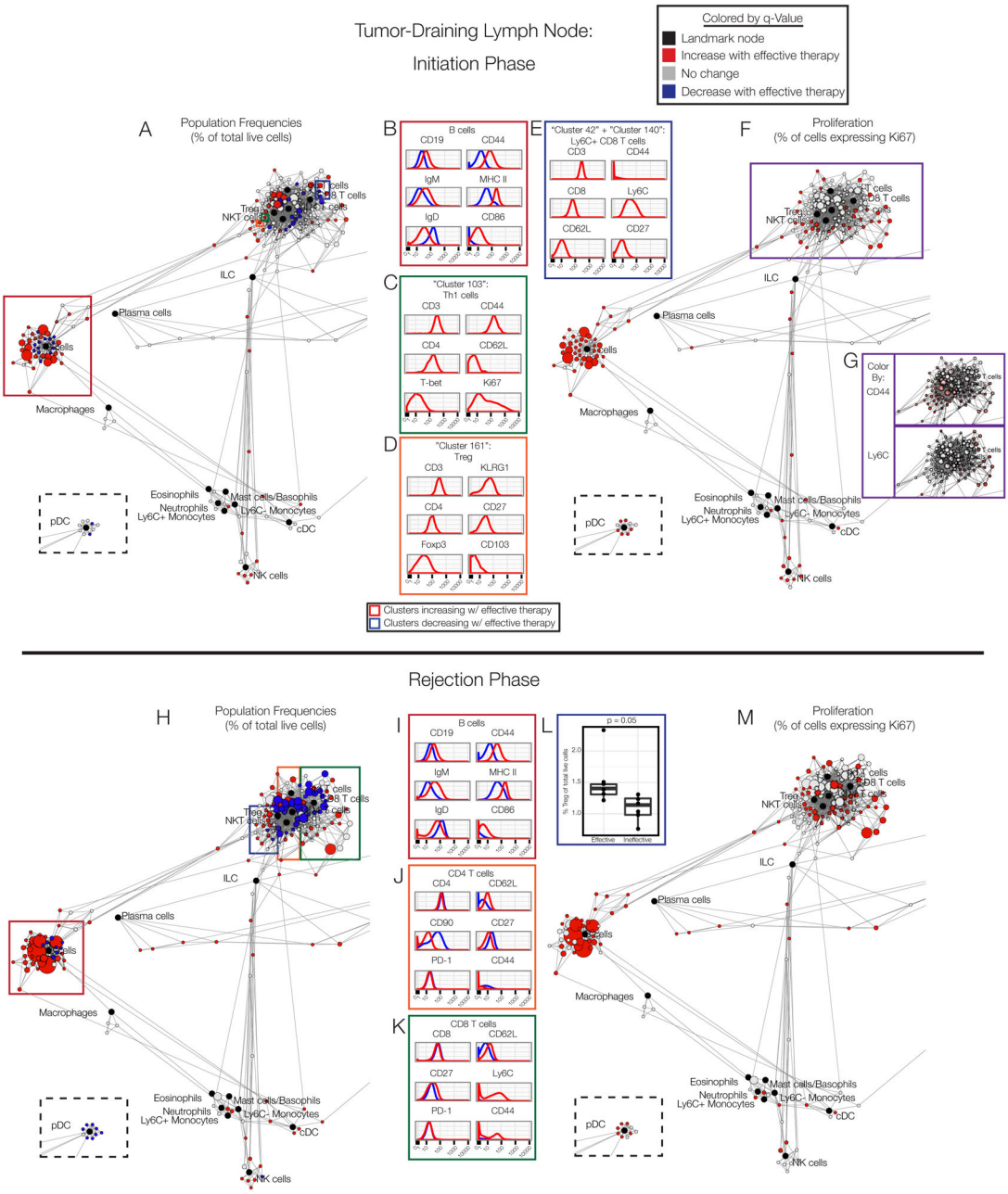

Figure 3. Cells in the tumor-draining lymph node display sustained activation

(A) Scaffold map of the draining lymph node on day 3. (B) Expression profile of B cell clusters expanding with effective therapy (red) versus those not changing (black). (C) Expression profile of Th1, (D) Treg or (E) CD8 T cell clusters increasing with effective therapy. (F) Scaffold map of Ki67 expression in cells in the draining lymph node on day 3. (G) Expression of CD44 and Ly6C in T cell clusters. (H) Scaffold map of the draining lymph node on day 8. (I) Expression profile of B cell, (J) CD4 T cell or (K) CD8 T cell clusters expanding with effective therapy (red) versus those decreasing (blue). (L) Frequency

of Treg clusters. (M) Scaffold map of Ki67 expression in the draining lymph node on day 8. See also Fig. S4–S5, Tables S2–S3.

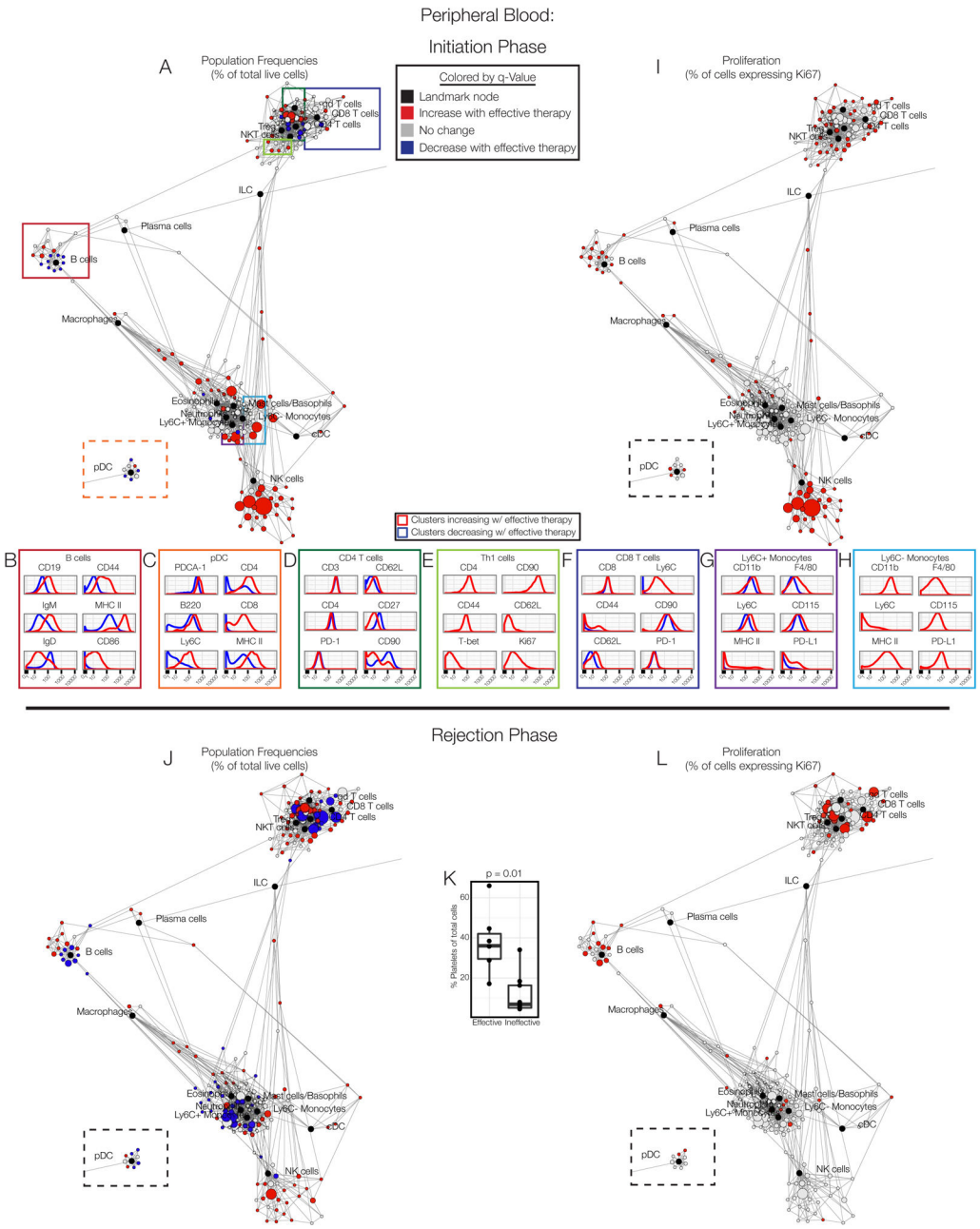

Figure 4. Immune responses are sustained in peripheral blood

(A) Scaffold map of blood on day 3. (B) Expression profile of B cell, pDC, (D) CD4 T cell, (E) Th1 cell,. (F) CD8 T cell, (G) Ly6C+ monocyte, or (H) Ly6C- monocyte clusters expanding with effective therapy (red histogram) versus those decreasing (blue histogram). (I) Scaffold map of Ki67 expression in immune cell clusters in blood on day 3. (J) Scaffold map of blood on day 8. (K) Frequency of platelets on day 8. (L) Scaffold map of Ki67 expression in cells in blood on day 8. See also Fig. S4, S6, Tables S2–S3.

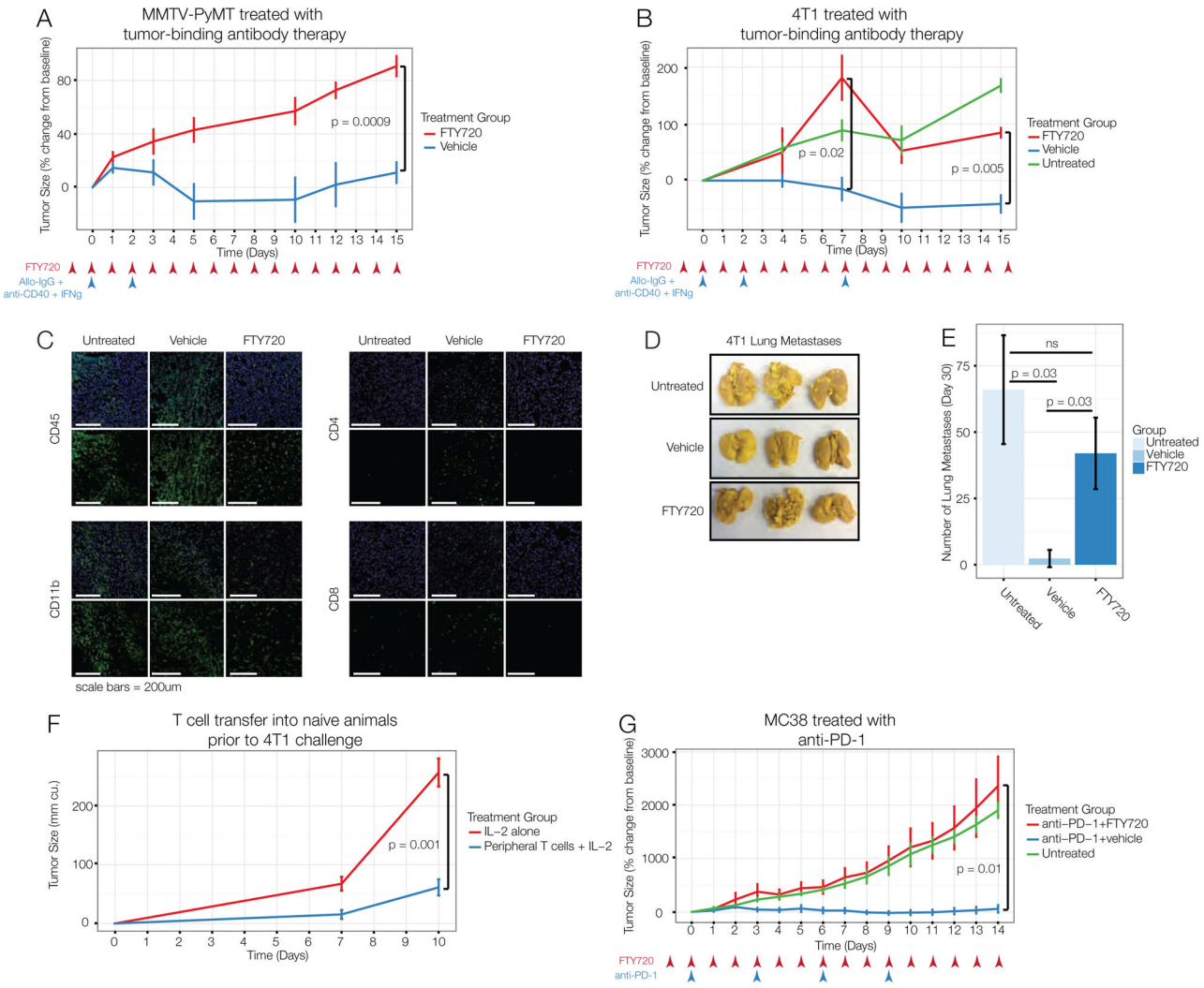

Figure 5. Interfering with systemic immune responses prevents effective immunotherapy

(A) MMTV-PyMT tumor-bearing mice treated with alloIgG, anti-CD40, IFNγ and daily FTY720 or ethanol control starting one day before therapy. (B) Mice with orthotopic 4T1 tumors treated as in A. (C) Immunofluorescence of 4T1 tumors 14 days after therapy. (D–E) 4T1 lung metastases 20 days after therapy. (F) T cells from spleen and lymph nodes of mice with 4T1 tumors, treated with alloIgG, anti-CD40, IFNγ and FTY720 were transferred with IL-2 into naïve Balb/c mice. Controls only received IL-2. Recipients were challenged s.c. with 4T1 cells the next day. (G) MC38 tumor-bearing mice untreated or treated with anti-PD-1 and ethanol control or FTY720. All p-values reflect two-tailed, heteroskedastic t-tests in R. Error bars represent S.D.

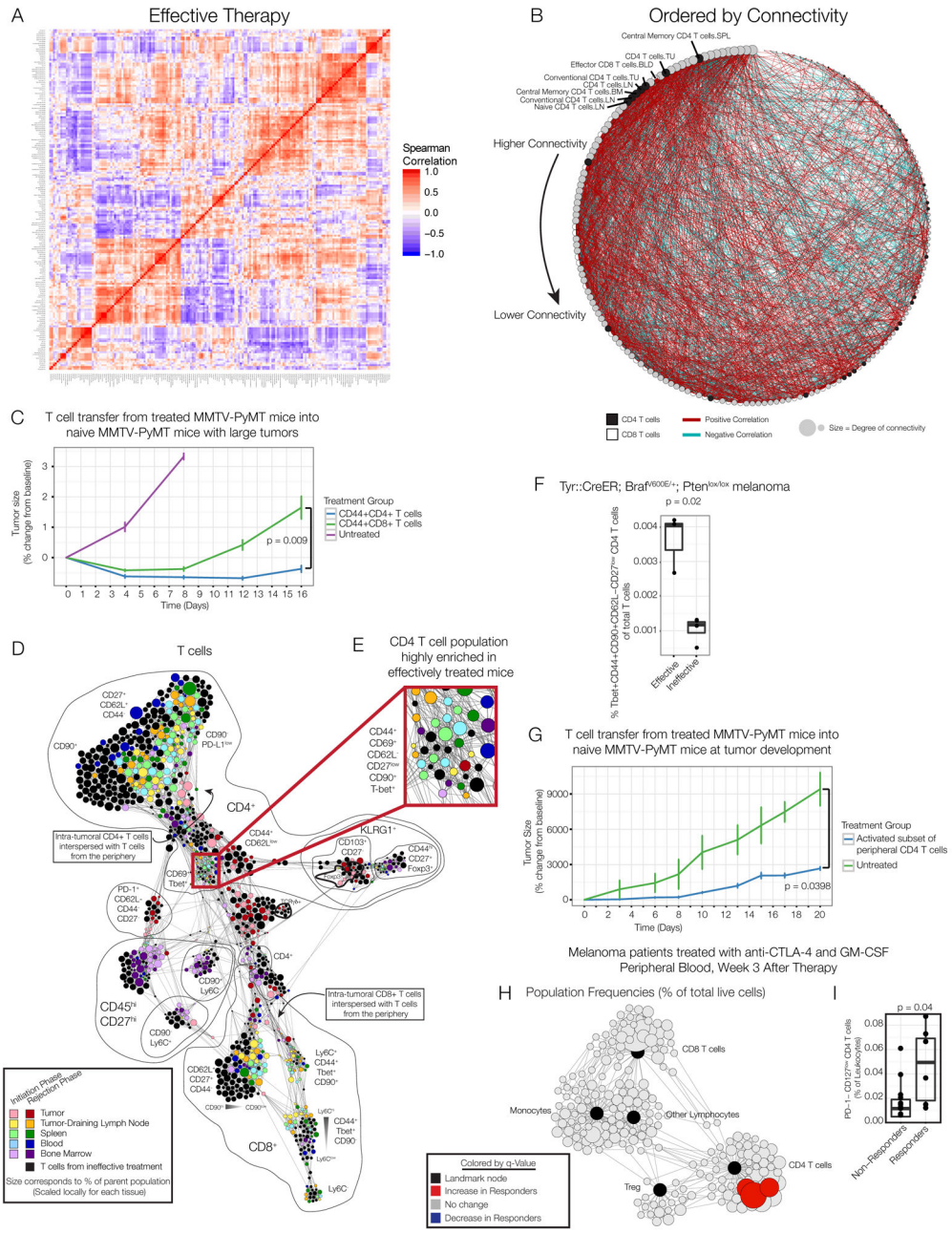

Figure 6. A CD4 T cell subset from the periphery is sufficient to mediate anti-tumor immunity

(A) Pairwise correlations and hierarchical clustering of immune cell frequencies across organs of mice treated with effective therapy. (B) Adjacency matrix from panel A ordered by connectivity. CD4 T cells in black; CD8 T cells in white. (C) CD44+ CD4 or CD8 T cells from the lymph node, spleen and blood of MMTV-PyMT mice treated with effective therapy were expanded and transferred into treatment-naïve MMTV-PyMT mice (n=3–4 per group). (D) Force-directed graph of T cells from each tissue, time and treatment. Colored by tissue of origin. Light colors indicate initiation phase; dark colors indicate rejection phase. Clusters from mice receiving no or ineffective therapy are black. Node size reflects the frequency of

T cells in that cluster as a percent of T cells by tissue. (E) CD4 T cells enriched in the periphery after effective therapy. (F) Frequency of Tbet+CD44+CD62L-CD27^{low} CD4 T cells in the draining lymph node of BP melanoma mice on day 8. (G) CD44+CD62L-CD27^{low} CD4 T cells were isolated from the lymph node, spleen and blood of MMTV-PyMT mice treated with effective therapy. Treatment-naïve MMTV-PyMT mice were sublethally irradiated, and sorted T cells (n=4) or PBS control (n=3) was injected i.v. All p-values reflect two-tailed, heteroskedastic t-tests in R. Error bars represent S.D. (H) Scaffold map of flow cytometry data from blood of melanoma patients treated with anti-CTLA-4 antibodies and GM-CSF, 3 weeks after therapy began. Red nodes are cell subsets significantly expanded in responding patients compared to non-responders. (I) Frequency of CD4+PD-1-CD127^{low} T cells (identified manually) of total leukocytes, analyzed by two-tailed Wilcoxon rank-sum test. See also Fig. S7.

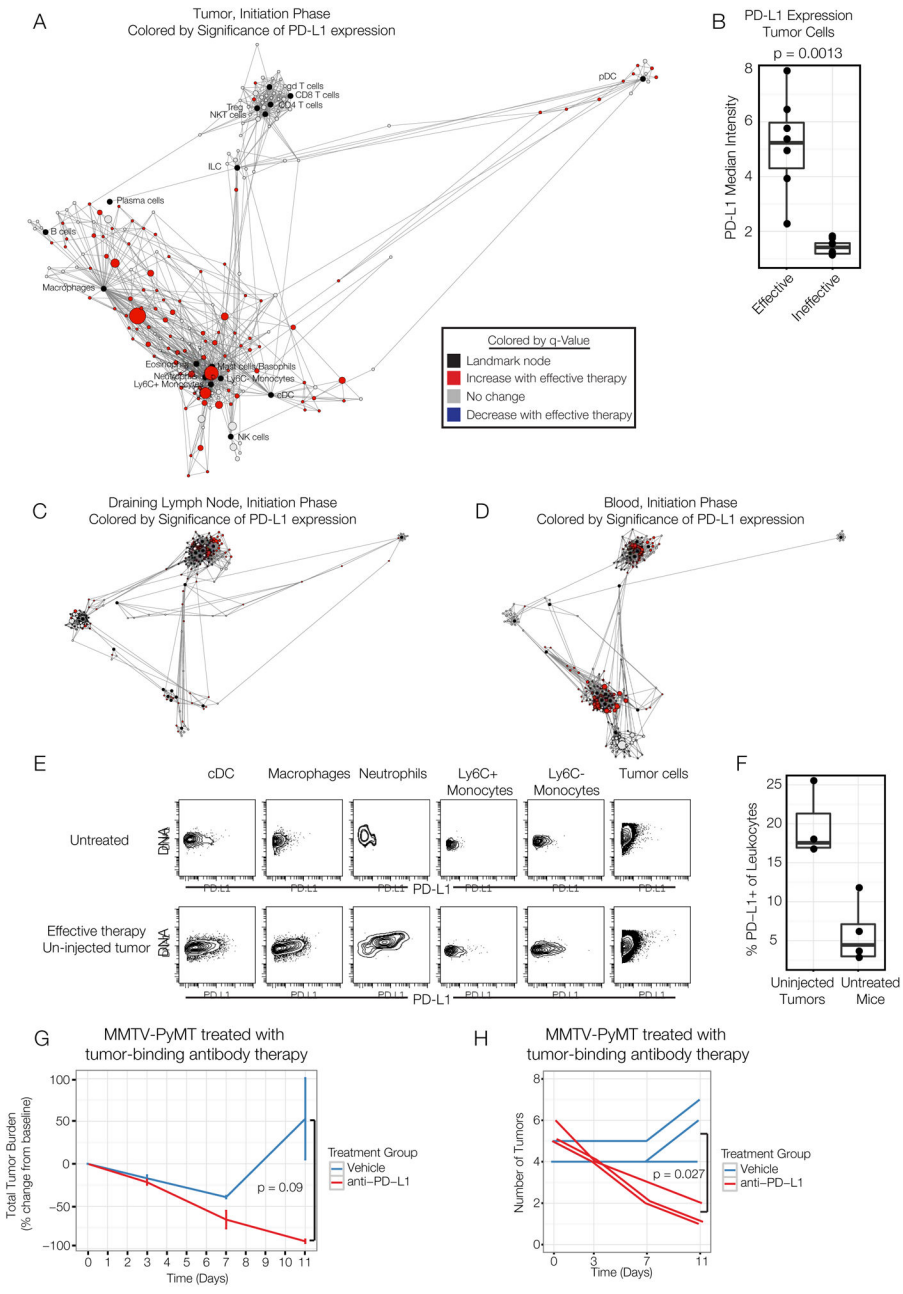

Figure 7. PD-L1 blockade combined with tumor-binding antibody therapy enables distal tumor rejection in multifocal disease

(A) Scaffold map denoting PD-L1 expression in immune cells in the tumor between effective and ineffective groups on day 3. (B) Percent of tumor cells expressing PD-L1 on day 3. (C) Scaffold maps representing changes in PD-L1 expression in the draining lymph node or (D) blood. (E) PD-L1 expression in un-injected tumors in MMTV-PyMT mice with multi-focal disease on day 3. (F) Frequency of PD-L1+ leukocytes in un-injected tumors of treated or untreated mice. (G) Tumor burden in MMTV-PyMT animals with late-stage multi-focal disease after tumor-binding antibody therapy alone or in combination with systemic

anti-PD-L1. (H) Number of palpable tumors in mice from G. All p-values reflect two-tailed, heteroskedastic t-tests in R. Error bars represent S.D.